This is a preprint, the final version is subject to change, of the American Mineralogist (MSA)
Cite as Authors (Year) Title. American Mineralogist, in press.
DOI: https://doi.org/10.2138/am-2019-6759

Revision 1

Crystal Size Distribution of Amphibole Grown from Hydrous Basaltic Melt at 0.6-2.6 GPa and 860-970 °C

BO ZHANG[1, 2, 3], XIANXU HU[4], PAUL D. ASIMOW[3], XIN ZHANG[1], JINGUI XU[1], DAWEI FAN[1,*], AND WENGE ZHOU[1]

[1] Key Laboratory for High Temperature and High Pressure Study of the Earth's Interior of Institute of Geochemistry, Chinese Academy of Sciences, Guiyang 550081, China

[2] University of Chinese Academy of Sciences, Beijing 100049, China

[3] Division of Geological and Planetary Sciences, California Institute of Technology, Mail Code 170-25, Pasadena, California 91125, USA

[4] Guizhou University of Finance and Economics, Guiyang 550025, China

ABSTRACT

We carried out three series of amphibole crystallization experiments from hydrous basaltic melt in order to calibrate the dependence of crystal growth rate on temperature and pressure in amphibole-bearing igneous rocks. One series of 100-hour duration multi-anvil experiments were carried out at constant pressure of 0.6 GPa and variable temperature, 860 °C to 970 °C. The second series was conducted at constant temperature of 970 °C and variable pressure from 0.6 GPa to 2.6 GPa. The third series examined the time dependence at 970 °C and 0.6 GPa, with durations from 1 to 100 hours. A verification experiment showing both reproducibility and the ability of these three series to predict behavior at novel conditions was performed in a piston cylinder at 1.0 GPa and 900 °C for 63 h. All experiments yielded mostly amphibole in a quenched glass of granitic to granodioritic composition. We used the two-dimensional thin section method to measure the crystal size distribution (CSD) of amphibole in the experimental products. Concave-down CSD curves at small sizes indicate a textural coarsening process during the crystallization. The CSD data were inverted using canonical CSD theory for CSD growth rate; maximum and average growth rates of amphibole were also inferred directly from maximum and average grain size and crystallization time. Maximum growth rate is, of course, always larger than average growth rate, which is in turn slightly larger than CSD growth rate,

suggesting that CSD growth rate is an adequate measure of the average growth rate of a mineral in magmatic rocks. The CSD growth rate increases with increasing temperature in the isobaric series and with increasing pressure at constant temperature. However, the growth rate is negatively correlated with crystallization time at constant temperature and pressure. Based on the experimental results, a functional form for evaluating growth rate at known pressure and temperature from an observed amphibole CSD was developed and applied to a diorite collected from the eastern Tianshan Mountains, Xinjiang Uygur autonomous region, NW China. The estimated growth rate of amphibole is between 1.6×10^{-9} mm/s and 5.6×10^{-7} mm/s, and combined with petrological constraints on pressure and temperature, the corresponding crystallization time was between 0.1 and 4.3 years in the natural diorite.

Keywords: Amphibole, Basalt, High temperature-High pressure, Crystal size distribution, Growth rate, Crystallization time

INTRODUCTION

The habits, textures, and sizes of crystalline phases in magmatic rocks preserve essential information about the conditions and processes accompanying their crystallization. In particular, the statistical distribution of grain sizes, the crystal size distribution (CSD), can provide insight into magma crystallization kinetics and may give information on the growth rates of minerals and on magma residence times. Numerous studies have pursued this idea and its applications in igneous and metamorphic petrology since its initial development by Marsh (1988) (e.g., Cashman and Marsh 1988; Cashman and Ferry 1988; Zieg and Marsh 2002; Azpiroz and Fera´ndez 2003; Higgins 2006a; Mujin et al. 2017; Silva et al. 2017). These studies generally use one of two approaches, whereby crystal growth rate is either directly derived from measured 2D grain intersection size and an estimate of crystallization time (the so-called 2D measurement approach) or estimated from CSD theory (e.g., Marsh 1988; Hammer and Rutherford 2002; Cabane et al. 2005; Brugger and Hammer 2010; Arzilli et al. 2015; Zellmer et al. 2016).

Past CSD studies have focused on the minerals plagioclase (e.g., Kirkpatrick 1977; Cashman and Marsh 1988; Cashman 1993; Pupier et al. 2008; Vona and Romano 2013; Fornaciai et al. 2015), olivine (e.g., Mangan 1990; Armienti et al. 1991; Ni et al. 2014), and pyroxene (e.g., O'Driscoll et al. 2008; Ni et al. 2014). The most common application of CSD investigations of these minerals in magmatic rocks has been to estimate crystal nucleation and growth mechanisms and hence to constrain magma residence time or solidification and cooling rate in magma chambers (e.g., Mangan 1990; Cashman 1993; Lentz and McSween 2000; Turner et al. 2003; Piochi et al. 2005; Brugger and Hammer 2010; Yang 2012). For instance, Cheng et al. (2014) measured the CSD of plagioclase megacrysts in the Panzhihua layered gabbroic intrusion from the Emeishan large igneous province (LIP), SW China, and obtained a quantitative estimate of the crystallization period, 530-8118 years. From this result, these authors concluded that the timescale of emplacement of the layered gabbro was at least 530 years and more likely several millennia.

The use of CSD data to interpret natural rocks, however, is dependent on extensive experimental studies to define empirical parameters and calibrate growth rate laws (e.g., Dunbar et al.1995; Pupier et al. 2008; Orlando et al. 2008; Vona and Romano 2013; Mills and Glazner 2013; Ni et al. 2014). For example, using

CSD measurements, Pupier et al. (2008) showed that the average growth rate of plagioclase from basalt at atmospheric pressure and about 1190 °C is 10^{-8} mm/s at a low cooling rate of 0.2 °C/h and 10^{-7} mm/s at a high cooling rate of 3 °C/h. Vona and Romano's (2013) experiments on plagioclase growth in basalt at atmospheric pressure and 1131-1187 °C showed that nucleation density and nucleation rate are directly proportional, whereas growth rate is inversely proportional, to the degree of undercooling. However, experimental studies of CSD development at elevated pressure have been quite limited. Published results include those of Larsen (2005), reporting experimental growth of An_{28-38} plagioclase rims from rhyodacite at 0.05-0.15 GPa and 825-880 °C, yielding rates between $3.5(\pm0.3)\times10^{-9}$ mm/s and $6(\pm2)\times10^{-8}$ mm/s. Subsequently, Brugger and Hammer (2010) found that plagioclase growth from hydrous rhyodacite upon decompression from 880 °C and 130 MPa was, on average, faster by a factor of ~5 upon rapid decompression (2 MPa/h) compared to slow decompression (0.5 MPa/h).

Uses of amphibole for CSD studies have been quite sparse, despite the importance of amphibole as an igneous rock-forming mineral in intermediate rock series. Higgins and Roberge (2003) verified that the CSD of amphibole in the andesite of the Soufrière Hills Volcano, Montserrat, is consistent with the textural coarsening model but did not estimate crystallization parameters such as growth rate or crystallization time. The only experimentally determined growth rate for amphibole, 5.0×10^{-7}-1.0×10^{-6} mm/s, was estimated from long axes of amphiboles in 2-4 h duration experiments on water-saturated Shiveluch Volcano (Kamchatka) andesite at 950 °C and 0.2 GPa (Simakin et al. 2009). Certainly, further studies to calibrate application of the CSD of amphibole at high temperature and pressure are needed.

Another critical issue in the use of CSD theory to interpret growth rate is the nearly universal, and rarely verified, assumption of constant crystal growth rate (e.g., Marsh 1988; Cashman and Marsh 1988; Cashman 1988; Mangan 1990; Armienti et al. 1991, 1994; Lentz and Mcsween 2000; Vona and Romano 2013; Fornaciai et al. 2015). A few investigators (e.g., Gondé et al. 2006; Schiavi et al. 2009; Ni et al. 2014) have argued, on the basis of *in situ* observation, that the growth rates of minerals crystallizing from melts are not constant; grain coarsening is an example of a size-dependent growth process. This suggests that it remains necessary to directly compare, whenever possible, the growth rate inferred from CSD theory with that from

the method of 2D measurement, and to do so over a range of times and grain sizes.

In this work, we therefore present a preliminary study of amphibole growth from a hydrous basaltic melt at pressures 0.6-2.6 GPa, temperatures 860-970 °C, and crystallization times 1-100 h. The two-dimensional thin section method was adopted both for direct measurement of 2D crystal sizes and for estimation of the CSD. We extract the temperature and pressure dependences of amphibole CSD evolution and crystal growth rate and we directly compare the growth rates deduced from CSD theory and from 2D measurement. We then apply the inferred amphibole growth rate as a function of temperature and pressure to estimate the crystallization time of amphibole in a diorite with good petrological constraints on crystallization conditions, from the eastern Tianshan Mountains, Xinjiang Uygur autonomous region, NW China.

EXPERIMENTS

Starting material

The starting material for the crystallization experiments is a natural basalt with modal mineralogy plagioclase (40%), iddingsitized olivine (25%), clinopyroxene (20%), glass (10%) and minor iron titanium oxide (5%) from the Yichuan-Ruyang region in west Henan province, China. Hydrous alteration products host enough water to make this a suitable starting material for crystallization experiments appropriate to magmas with primary dissolved water; bulk composition and water content are given in Table 1 (Zhou et al. 1998). The rock sample was repeatedly crushed until all fragments passed through a 200 mesh sieve. The coarse-grained powder was then ground under ethanol in an agate mortar to a particle size of ～15 μm. Finally, the sample was heated for more than 10 h at 200℃ in a muffle furnace to minimize adsorbed water.

Experimental procedures

Three series of experiments (temperature series, pressure series, and time series) were performed in the multi-anvil apparatus and one complementary experiment was performed in the piston cylinder. The experimental protocol and configuration of charges for multi-anvil experiments were similar to those described by Zhou et al. (1999), with two significant differences in the assembly. This study used graphite, (rather than stainless steel sheet) heating elements to obtain more uniform temperatures and Al_2O_3 insulating tubes both inside and outside the heater to better encapsulate water. Fine-ground powder samples were

loaded into 3 mm long graphite containers with inner diameter 4 mm and placed between 1 mm thick graphite discs at each end. The pressure transmitting medium was pyrophyllite. In the additional piston cylinder experiment, the graphite capsule was 3 mm long with an inner diameter of 2 mm and the pressure transmitting medium was calcium fluoride. All complete assemblies were heated for more than 10 h at 200 °C in a muffle furnace before loading into the apparatus.

The multi-anvil apparatus used is in the Key Laboratory for High Temperature and High Pressure Study of the Earth's Interior of the Institute of Geochemistry, Chinese Academy of Sciences. The piston cylinder is in the Division of Geological and Planetary Sciences, California Institute of Technology. The pressure of the multi-anvil apparatus was calibrated at high pressure and temperature against the melting curves of Au (Fu and Zhu 1980) and four other metals (Cu, Al, Pb, and Zn) (Shan et al. 2007). The pressure of the piston cylinder was calibrated at two points against the stability limits of kushiroite ($CaAl_2SiO_6$ pyroxene) using the phase diagram assessment of Gasparik (2003). The temperatures were measured and controlled with $W_{95}Re_{05}$-$W_{74}Re_{26}$ thermocouples placed at the top of the graphite capsules. No correction was applied for the effect of pressure on the electromotive force of the thermocouple. The accuracy of experimental pressure and temperature were ±0.05 GPa and ±5 °C, respectively. In the “temperature series”, charges were held above the liquidus at 0.6 GPa and 1460 °C for 1 h, then rapidly cooled isobarically to crystallization temperatures of 860 °C, 915 °C, or 970 °C, and held for 100 h before quenching. In the “pressure series”, the charges were brought to superliquidus conditions (1460 °C and 0.6 GPa, 1490 °C and 1.1 GPa, 1515 °C and 1.6 GPa, 1540 °C and 2.1 GPa, or 1570 °C and 2.6 GPa) for 1 h, and then rapidly and isobarically cooled to a uniform crystallization temperature of 970 °C and held for 100 h. In the “time series”, charges were held at 0.6 GPa and 1460 °C for 1 h, then rapidly cooled isobarically to the crystallization temperature of 970 °C, and held for 1 h, 10 h, 60 h, or 100 h before quenching. Finally, in order to verify the reproducibility of the multi-anvil experiments and the utility of the pressure series and temperature series for extrapolating to other conditions, an additional piston cylinder experiment was done with initial 1 hour hold at 1.0 GPa and 1370 °C, rapid isobaric cooling to 900 °C, and crystallization time 63 h (the experiment was terminated before 100 h by a thermocouple failure). According to alphaMELTS (Smith and Asimow, 2005), the

water-undersaturated liquidus of the starting material increases from 1150 °C at 0.6 GPa to 1500 °C at 2.6 GPa. The liquidus calculation was verified by direct observations and bracketed between 1200 °C and 1215 °C by several experiments at 1.0 GPa and 1 h. Glass quenched directly after 1 h at superliquidus conditions was free of crystals or crystallites at the limit of back-scattered electron (BSE) imaging scale. Hence, we are confident that each crystal growth experiment began from a state in which all crystal remnants and nuclei were destroyed at time zero. All samples were quenched by shutting off the electric power. Experimental conditions are summarized in Table 2.

Analytical techniques and CSD measurement

BSE images of polished surfaces of recovered charges from all multi-anvil experiments were acquired with the EPMA-1600 electron microprobe at the Institute of Geochemistry, Chinese Academy of Sciences, and phase compositions were analyzed with the JEOL JXA-8100 electron microprobe at the Institute of Geology and Geophysics, Chinese Academy of Sciences. A 15 kV, 20 nA beam was focused to diameter 1-5 μm for minerals and 10 μm for glass. The BSE images and chemical compositions in the additional experiment were acquired with the JEOL JXA-8200 electron microprobe at Division of Geological and Planetary Sciences, California Institute of Technology. Operating conditions were similar to the previous conditions but the beam diameter was 0.5 μm for both the minerals and melt. Na and K were counted in the first pass to reduce the problem of Na and K loss during analyses (Morgan and London 2005). Major element compositions of amphiboles and glass in the experimental products are reported in Table 2.

Quantitative textural analyses can be performed using either two-dimensional sections, partial three-dimensional reconstruction from serial sections, or fully three-dimensional X-ray tomography images. However, the two-dimensional section method is the simplest and is widely used in quantitative textural analysis (e.g., Castro et al. 2003; Higgins and Roberge 2003; Morgan and Jerram 2006; Jerram et al. 2009; Yang et al. 2010; Berger et al. 2011). Here, we use two-dimensional sections to measure the CSD of the amphibole in our experimental products, following the procedure of Yang et al. (2010): (1) acquire BSE images of polished sections of each experimental product using electron microprobe (Fig. 1); (2) process contrast and brightness of these BSE images in Adobe Photoshop CS6 and select a threshold grayscale value

to make a binary image (an example, RUN#10084-3, is shown in Fig. 2); (3) manually separate touching crystals with a narrow non-crystal line and analyze the binary images in ImageJ (version 1.45s) to determine the number of crystals and the long and short axes and area of the best-fitting ellipse for each crystal (Table 4, Herwegh 2000); (4) obtain the best-fit three-dimensional shape of the population of crystals using CSDslice (version 5) (Morgan and Jerram 2006) (Fig. 3a, Table 4), expressed as S/I vs. I/L, where S=Short dimension, I=Intermediate dimension, L=Long dimension (Fig. 3b); and (5) calculate the CSD of amphibole based on the short axes of the best fitting ellipses using CSDCorrections 1.40 (Higgins 2000).

EXPERIMENTAL RESULTS

Phase assemblages and compositions

All the experimental phase assemblages are dominated by amphibole (*Amp*) and glass (*Gl*). Some experiments also include accessory apatite (*Apa*), spinel (*Sp*), albite (*Ab*) or ilmenite (*Ilm*), based on optical polarizing microscope observations, BSE images and major element analyses (Fig. 1, Table 2). Clinopyroxene, orthopyroxene, and olivine are absent and amphibole is a sufficiently dominant rock-forming stable phase that these experiments can be taken as single-solid free growth experiments. The run products contain about 35-58% *Amp* crystals with easily observed, distinct boundaries against glass (Fig. 1). The crystal fractions vary as expected with decreasing temperature or increasing pressure and do not appear, even in the lowest temperature run, to have reached any limit on the of amount of amphibole that can crystallize from the starting composition; hence we do not consider that the closure effect discussed by Higgins (2002a) is an issue affecting the interpretation of CSDs in these experiments. *Amp* grain sizes range from 0.0001 mm in RUN# 10084-8 (0.6 GPa, 970 °C and 1 h) to 1.44 mm in RUN# 10084-7 (2.6 GPa, 970 °C and 100 h). The crystal forms become increasingly euhedral with increasing temperature or pressure at equal time or with increasing time under isothermal-isobaric conditions. The shape of amphibole changes from bladed to prismatic with increasing temperature or time and possibly from bladed towards tabular with increasing pressure (Fig. 3b). BSE images reveal that some optically continuous *Amp* grains are zoned into domains of differing contrast (Fig. 1g and Table 2). *Amp* crystal chemical formulae were calculated according to the recommendations of Hawthorne et al. (2012) and reported in Table 3. All the experimental

amphiboles belong to the calcic amphibole category; most are classified as Ti-rich pargasite/sadanagaite and have $Mg^{\#}$=50-60. The melt in each experiment quenched to a clean glass and their compositions are broadly granitic to granodioritic (Table 2).

CSD of amphibole

Figure 4 shows that the crystal size distribution curves (CSDs) for amphibole, plotted as logarithm of population density (n) vs. size (L), are concave down at small sizes and nearly linear at larger sizes in each experimental product of both the temperature series and the pressure series. The boundary between the concave and linear domains increases with increasing temperature and pressure, from <0.01 mm at 0.6 GPa and 860 °C to 0.14 mm at 2.6 GPa and 970 °C. These CSD shapes match the lognormal distribution (L-CSD) predicted by the theory of Higgins (2006b). However, the CSDs for amphibole in the time series are not obviously concave down at small sizes, especially at the shortest crystallization time (Fig. 4c). The time series shows that the CSD curve starts out steep and linear and then evolves to a concave down form at small sizes as time increases from 1 hour to 100 hours.

The maximum size of amphibole (L_{max}, defined as the average length of the four largest amphibole crystals in each experimental product, after Boorman, et al. 2004 and O'Driscoll et al. 2008) is 0.09 mm at 860 °C and increases to 0.39 mm at 970 °C in the temperature series (Table 4), but L_{max} in piston cylinder run R461, 0.04 mm, is smaller than expected from the 100 hour runs, presumably due to its shorter duration. L_{max} also increases in the pressure series and time series, from 0.39 mm at 0.6 GPa to 0.94 mm at 2.6 GPa and from 0.03 mm at 1 h to 0.39 mm at 100 h, respectively (Table 4). The negative slopes of the linear portions of the semi-logarithmic CSD curves are systematically correlated with temperature and pressure. Because the experimental CSDs are nearly linear over significant intervals, the crystallization parameters of the Marsh CSD model, nucleation density, nucleation rate, and growth rate, can be calculated with apparently good precision by linear fitting to obtain intercept and slope. We excluded the data shown as filled symbols in Fig. 4, namely points from the concave-down interval at small size in each experiment as well as points with large uncertainty (these bins contain fewer than five crystals) at the very upper ends of some CSDs (e.g., Higgins 2000; Mock and Jerram 2005; Yang 2012). These points are an inevitable result of the

intersection-probability effect for the 2D CSD (Higgins 2000); exclusion of these data is standard practice when fitting CSD data, as described in many studies (e.g., Mock and Jerram 2005; Yang 2012).

DISCUSSION

Explanation of the shape of the CSD curve

Marsh (1988) developed a theory for crystallization in a steady-state flow-through reactor, with continuous addition of fresh liquid and removal of partly crystallized material. This model leads to an expected relation between population density (n), nucleation density (n^0) and growth rate (G),

$$n = n^0 \exp[-L/G\tau], \quad (1)$$

where L is crystal size and τ is the average crystal characteristic time in the system. The nucleation rate (J) is determined by the nucleation density and growth rate:

$$J = n^0 G. \quad (2)$$

The intercept $\ln(n^0)$ and slope k of the CSD are determined by linear regression of a plot of $\ln(n)$ vs. L, over the range where the CSD is linear in a semi-log plot:

$$\ln(n) = \ln(n^0) + kL, \quad (3)$$

$$k = -1/G\tau. \quad (4)$$

Although the CSD theory of Marsh (1998) was developed for open systems, it also predicts a linear CSD at early times in a batch system (Marsh 1998).

However, the Marsh theory applies only to simple nucleation and growth in the open system and describes only linear CSDs. A closed-system experiment that yields concave-down CSDs must have experienced additional processes that limit the validity of interpreting their results with Marsh theory. These experiments have time for crystals to undergo textural maturation (Ostwald ripening; Voorhees 1992) or coarsening (Marsh 1988). These textural equilibration processes are driven by surface energy reduction. Smaller crystals, with higher specific surface energy, will dissolve and larger crystals will grow. Such textural equilibration most strongly and rapidly consumes small crystals, leading to CSD curves that are concave-down at small sizes and linear at larger sizes. The consequence of such maturation is that the intercepts obtained by linear fitting to the straight segments of texturally matured CSD are significantly in

error, erasing information about the nucleation rate, whereas the slopes are robust, such that the CSD growth rate can still be meaningfully obtained.

Similar CSD shapes have been explained by a temperature oscillation model (Simakin and Bindeman 2008; Higgins 2011), but the experimental temperatures were fixed in the present case. Hence, the classical Lifshitz–Slyozov–Wagner model (LSW, Lifshitz and Slyozov 1961) and the Communicating Neighbors model (CN) (Dehoff 1991; Higgins 1998) offer more reasonable means of analyzing this behavior.

The LSW equation assumes that all the crystals in the population are in perfect communication as the system minimizes its free energy. It predicts that small grains will be preferentially dissolved in favor of grains just larger than the critical size. Evolution subject to the LSW equation predicts progressive decrease in the population of small grains, gradual increase in the minimum size of the linear regime and no change at all in the slope of the line at larger sizes (schematically shown in Fig. 5a). On the other hand, the CN equation presumes that each large crystal is surrounded by a shell of small crystals and that communication is short-range. Although this model also predicts dissolution and disappearance of small crystals, the local increase in supersaturation of the mineral component allows crystals larger than the critical size to continue growing. An initially straight CSD evolving subject to this equation will become concave down at small sizes, the lower limit of the linear regime will rapidly increase, and the linear regime at all larger sizes will rotate towards shallower slopes and lower intercepts (Table 4, Fig. 5b; Higgins 1998, 2002a; Pupier et al. 2008). The CN equation has been a popular basis for interpreting CSDs of in natural rocks. For example, Higgins (2002b) argued that the size distributions of plagioclase, olivine, and clinopyroxene in the Kiglapait layered mafic intrusion (Labrador, Canada) were best explained by CN-type textural coarsening during slow cooling of an intrusion surrounded by warmed country rock.

Our closed-system experiments are simpler to interpret than natural magmas. Uncomplicated by processes such as magma mixing, fractional crystallization, or crystal accumulation, the experiments form initial crystal populations by a simple nucleation and growth process. Then, during the isothermal hold segment of our experiments, small crystals are consumed in favor of large crystals by textural coarsening, resulting in CSD curves with concave-down segments at small sizes in the temperature and pressure series

(Fig. 4a, b). The time series shows that at short times the CSD curves are not concave-down at small sizes; they start steep and linear (or even slightly concave-up) and evolve both towards concave-down shapes at small sizes and progressively shallowing linear segments at large sizes (Fig. 4c). Furthermore, the CSD curves of the temperature series clearly indicate that the linear segments do rotate to shallower slopes and lower intercepts with increasing temperature (Fig. 4a), which appears consistent with the predictions of the CN equation (Fig. 5b).

Influence of temperature on amphibole growth

In the temperature series, the maximum amphibole size (L_{max}: the average of the four largest intersection lengths of crystals in each product) after isobaric crystallization for 100 h increases from 0.09 mm at 860 °C to 0.39 mm at 970 °C, whereas the average size ($L_{av.}$: the average size of all crystal long axes) increase likewise from 0.01 mm to 0.08 mm (Table 4, Fig. 1a-c). The fit of CSD theory to these data predicts that, with increasing temperature, the amphibole growth rate (G_{CSD}) increases from 1.8×10^{-8} mm/s to 1.3×10^{-7} mm/s (Table 5). Thus, at constant pressure of 0.6 GPa and run duration of 100 h, maximum grain size, average grain size, and growth rate of amphibole are all positively correlated with crystallization temperature.

Amphibole crystal growth rate is a thermally activated kinetic process and so increases with rising temperature as long as the system remains below the liquidus temperature (e.g., Toramaru 1991; Orlando et al. 2008; Pupier et al. 2008). Both these behaviors are evident in the temperature series data. Moreover, the parameters extracted from piston cylinder experiment R461 (Fig. 1k), even given that the crystallization time is different, are consistent with multi-anvil experiment 10084-1: although the CSD growth rate of R461 is larger than that of 10084-1 due to the greater crystallization temperature, they are similar in magnitude.

Influence of pressure on amphibole growth

In the pressure series, L_{max} increases at constant temperature and time from 0.39 mm at 0.6 GPa to 0.94 mm at 2.6 GPa; the corresponding range of $L_{av.}$ is 0.08-0.23 mm (Table 4, Fig. 1c-g). The fit of the CSD lines yields as increase in G_{CSD} (from 1.3×10^{-7} mm/s to 4.2×10^{-7} mm/s, Table 5) with increasing pressure. Hence, at 970 °C and 100 h, crystal size and growth rate of amphibole are both positively correlated with

pressure.

In summary, the G_{CSD} increases from 1.8×10^{-8} mm/s to 4.2×10^{-7} mm/s with increasing temperature or pressure in the ranges 860-970 °C and 0.6-2.6 GPa, at constant crystallization time of 100 h. A preliminary relationship for G_{CSD} as a function of T and P from regression of these results, based on unweighted multiple linear regression, is expressed by (Fig. 6):

$$G_{CSD}(T, P) = 7.4(\pm3.8) \times 10^{-10}\ T + 1.4(\pm0.2) \times 10^{-7}\ P - 7.0(\pm3.5) \times 10^{-7}\ (R^2 = 0.96), \quad (5)$$

where T is expressed in °C and P in GPa. The simple bilinear functional form of this fit is adequate to reproduce the present data but lacks theoretical justification and should not be extrapolated beyond the calibrated range.

Influence of crystallization time on amphibole growth

In the time series, L_{max} after isothermal-isobaric crystallization increases from 0.03 mm at 1 hour to 0.39 mm at 100 hours while the $L_{av.}$ increases from 0.003 mm to 0.08 mm (Table 4, Fig. 1c, h-j). According to CSD theory, the amphibole growth rate (G_{CSD}) decreases from 7.6×10^{-7} mm/s to 1.3×10^{-7} mm/s with increasing crystallization time (Table 5). Thus, at constant temperature and pressure of 970 °C and 0.6 GPa, maximum and average grain size of amphibole are positively correlated with run duration, whereas growth rate is negatively correlated with these parameters and with time.

The results of the time series experiments show that the crystal growth rate is not constant over the course of finite degrees of crystallization, consistent with previous investigations (Schiavi et al. 2009; Ni et al. 2014). In the early stages of crystallization, crystals grow faster. With increasing crystallization time, the growth rate becomes slower as crystal sizes become larger. Therefore, the CSDs will rotate to shallower slopes and lower intercepts due to textural coarsening (Fig. 4c). The decrease in the intercept is rapid enough that apparent nucleation density and nucleation rate (which should be independent of experimental duration) change over the course of a time series at constant temperature and pressure. Hence, we do not attempt to interpret the fitted nucleation density or rate results; they are contaminated by the process of textural maturation in our closed-system experiments.

Comparison of growth rates from different methods

Constant growth rates are commonly assumed in applications of crystal size distribution theory, such that final crystal sizes and time below the liquidus are sufficient to estimate the growth rates (e.g., Marsh 1988, 1998; Lentz and Mcsween 2000; Vona and Romano 2013; Fornaciai et al. 2015). However, *in situ* observations of crystal growth in melt indicate that growth rate is in fact roughly proportional to grain size rather than uniform (e.g., Gondé et al. 2006; Schiavi et al. 2009; Ni et al. 2014). Moreover, the shapes of the CSDs in our experiments indicate that the crystals below a critical size grew and then subsequently dissolved during textural coarsening — a change in the sign of the growth rate! In the present case we do have a time series to examine this issue directly but, in the more common case when data are only available for a single crystallization time, some insight into this issue can be gained by comparing the growth rates derived from CSD theory with those from direct 2D measurements. We have three parameters indicating growth rate of amphibole in our experiments: G_{CSD} based on fitting the CSD theory to the linear segment of the CSD in the semilogarithmic plot, G_{max} based on largest crystal size and crystallization time, and $G_{av.}$ based on average crystal size and time (we note that data completeness at small sizes and statistical assessment show that the reported average crystal sizes are meaningful in this study; Higgins 2006a).

Plotted against temperature, pressure, or crystallization time, all the calculated growth rate parameters display the same correlations: increasing with temperature at constant pressure, increasing with pressure at constant temperature, and decreasing with time at isothermal-isobaric conditions. However, in all experiments, G_{CSD} is smaller than $G_{av.}$, which is in turn (by definition) smaller than G_{max}. Typically, the ratio of $G_{av.}$ to G_{CSD} is about 1.5 to 2 and the ratio of G_{max} to $G_{av.}$ is about 5. The best-fit value of G_{CSD} is always of the same order of magnitude as $G_{av.}$, but the precision of G_{CSD} is always much better, with uncertainty typically an order of magnitude smaller. The offset between G_{CSD} and $G_{av.}$ as well as the improved precision of G_{CSD} are readily understood, because G_{CSD} is calculated from the slope of the best-fit line excluding both the smallest and (usually) largest size bins in the CSD, whereas $G_{av.}$ is calculated from $L_{av.}$, which averages over all measured amphibole crystals in each experimental product. Because the amphibole CSD curves of the experimental products are concave down in the small size intervals, including these bins actually bias $G_{av.}$ to larger values than G_{CSD}. However, the irregular behavior of the textural maturation processes, compared

to the initial nucleation and growth stages, and the small number of crystals in the largest bin, lead to much larger uncertainty in $L_{av.}$ and hence in $G_{av.}$. Hence, we find that G_{CSD} from CSD theory is an excellent estimator of the average crystal growth rate in these experiments, similar in magnitude to the average growth rate but much more precise.

G_{max} and $G_{av.}$ of amphibole can be parameterized against T and P with quality of fit similar to G_{CSD}. The unweighted multiple linear regressions yield:

$$G_{max}(T, P) = 6.9(\pm1.8) \times 10^{-9}\, T + 8.8(\pm1.0) \times 10^{-7}\, P - 6.3(\pm1.6) \times 10^{-6}\ (R^2 = 0.97) \quad (6)$$

$$G_{av.}(T, P) = 2.1(\pm0.7) \times 10^{-9}\, T + 2.1(\pm0.4) \times 10^{-7}\, P - 1.9(\pm0.6) \times 10^{-6}\ (R^2 = 0.96). \quad (7)$$

Geological application

In a case where crystallization temperature and pressure are well-defined by petrologic criteria and are similar to the range calibrated in our experiments, the fits to our experiments, equations (5)-(7), can be used to estimate the growth rate of amphibole in a natural magmatic rock. Then, given observed crystal sizes, the growth rate estimates can be used to further estimate crystallization time. We apply this exercise, as an example, to estimate amphibole growth rate and crystallization time in a diorite that was collected from the Xiangshan complex in the eastern Tianshan mountains, Xinjiang Uygur autonomous region, NW China. The Xiangshan complex forms a major outcrop of the Huangshan-Jingerquan mafic-ultramafic belt of the Tianshan orogen, a Carboniferous-aged series of ultramafic rocks, gabbro and diorite (e.g., Xiao et al. 2010; Li et al. 2012). The major rock-forming minerals of diorite sample XS-4 are plagioclase (70%) and amphibole (25%). The principal minor mineral is titanite (5%).

Average crystallization temperature and pressure of the amphibole in diorite XS-4 can be estimated from a recent amphibole geobarometer (Ridolfi and Renzulli 2011), yielding 0.41±0.05 GPa. Next, the crystallization temperature is evaluated from amphibole thermometry (Putirka 2016), giving 908±28 °C. Our regression, equation (5), with these *T*-*P* estimates, then suggests that the G_{CSD} of amphibole in XS-4 should have been in the range 1.6×10^{-9}-5.7×10^{-8} mm/s. Likewise, G_{max} of amphibole, equation (6), is predicted to be between 8.9×10^{-8} and 5.6×10^{-7} mm/s and $G_{av.}$, equation (7), between 3.1×10^{-8} and 1.7×10^{-7} mm/s. Using any of these estimates, the growth rate of amphibole in XS-4 was about 10^{-9}-10^{-7} mm/s (Table 5).

The CSD of amphibole in XS-4 was measured using the same procedures applied to the experiments (Fig. 4d). Moreover, the crystallization time of the amphibole based on estimated G_{CSD} and grain size (2.16 mm based on short axes of best-fitting ellipses) is 0.12-4.28 years. The crystallization time of amphibole based on estimated G_{max} and the measured L_{max} (3.27 mm) is 0.18-1.17 years and that based on estimated $G_{av.}$ and measured $L_{av.}$ (1.17 mm) is 0.22-1.20 years (Table 4). By any of these estimates, the crystallization time of the amphibole is <5 years in XS-4. This result stands in stark contrast to crystallization times for plagioclase estimated previously for other igneous rocks; however, the result is roughly equivalent to the low range of estimates for olivine crystallization time in associated olivine-bearing gabbros (1-60 years, Vinet and Higgins 2011). Petrographic analysis shows that these estimates are not necessarily inconsistent. With a crystallization sequence olivine-plagioclase-amphibole in the overall plutonic complex, a plausible scenario is rapid cooling through the near-liquidus olivine growth interval, extended residence at intermediate temperatures dominated by plagioclase growth, and a short magmatic residence time after onset of amphibole crystallization near the solidus. This interpretation is preliminary, but together with quantitative models of enthalpy of crystallization (e.g., from alphaMELTS), it places strong constraints on the rate of heat loss from the pluton at each stage of crystallization.

IMPLICATIONS

Methodologically, there are a number of different ways to estimate crystal growth rates from textural analysis, and it is important to define best practices for consistent comparison among studies. In this study, we applied three different methods (CSD theory, average grain size measurement, and maximum grain size measurement). Growth rates estimated from CSD theory are consistently 1.5 to 2 times smaller, but an order of magnitude more precise, than growth rates based on average grain size, and about an order of magnitude smaller than those based on maximum grain size. Hence, average growth rates of amphibole are apparently best calculated from CSD theory.

The CSD growth rate increases with increasing temperature in the isobaric series and with increasing pressure at constant temperature. However, the growth rate decreases with increasing crystallization time at constant temperature and pressure.We find that the average and maximum grain sizes and CSD growth rate

also increase with the pressure. Apparently, directly or indirectly, pressure is a critical factor in the nucleation kinetics of amphibole. Hence a barometric estimate of crystallization conditions is necessary when applying our calibration of amphibole CSD to estimating crystallization rates and times in nature.

Numerous studies have documented how useful crystal nucleation and growth rates are as constraints on magma residence time and cooling rate in magma chambers (e.g., Cashman 1993; Lentz and McSween 2000; Piochi et al. 2005; Brugger and Hammer 2010; Yang 2012). Expanding the library of minerals that can be used for such analysis correspondingly expands the range of magma types whose crystallization rates can be obtained. The present study, by calibrating the growth rates of amphibole, is a major extension to hydrous intermediate magmas that may lack olivine or pyroxene and where feldspar may only grow during restricted parts of the crystallization history. The preliminary results suggest that the growth rate of amphibole in hydrous basaltic magma can be parameterized by simple bilinear dependence temperature and pressure.

Applying the amphibole CSD method to a natural diorite from the Tianshan orogen in NW China yields growth times for amphibole of 0.1-4.3 years. Crystallization times obtained from plagioclase CSD analysis in similar rocks are often much longer. If estimates from different minerals are interpreted naively as measurements of the total crystallization time of a pluton, then disagreements among times obtained from plagioclase and amphibole would appear to a serious issue, calling into question one or both of the growth rate estimates. However, each mineral can sample a different portion of the crystallization history because they saturate in the magma at different stages of evolution. We propose that application of CSD analysis to growth rates of different minerals within a given pluton, together with petrologic information on the crystallization sequence, may provide a unique insight into variations in the rate of cooling.

ACKNOWLEDGMENTS

The authors would like to thank Michael Zieg and Michael Higgins for their very insightful and thorough reviews, and sincere thanks are extended to Associate Editor Erik Klemetti. We wish to thank Hongfeng Tang for providing the important diorite sample, Neng Jiang for his assistance during EMP analyses. We warmly thank Yijin Yang and Wei Mao for their linguistic assistance during the preparation of this manuscript. This work benefited from the financial support of the National Natural Science Foundation of

China (Grant No. 41772043), the Joint Research Fund in Huge Scientific Equipment (U1632112) under cooperative agreement between NSFC and CAS, the Chinese Academy of Sciences "Light of West China" Program (Dawei Fan, 2017), Youth Innovation Promotion Association CAS (Dawei Fan, 2018), the Strategic Priority Research Program (B) of the Chinese Academy of Sciences (XDB 18010401), the CPSF-CAS Joint Foundation for Excellent Postdoctoral Fellows (Grant No. 2017LH014), and China Postdoctoral Science Foundation (Grant No. 2018M631104). Experiments in the Caltech lab and participation of PDA in this work were supported by the US NSF through award EAR-1550934.

REFERENCES CITED

Armienti, P., Innocenti, F., Pareschi, M.T., Pompilio, M., and Rocchi, S. (1991) Crystal population density in not stationary volcanic systems: estimate of olivine growth rates in basalts of Lanzarote (Canary Islands). Mineralogy and Petrology, 44, 181-196.

Armienti, P., Pareschi, M.T., Innocenti, F., and Pompilio, M. (1994) Effects of magma storage and ascent on the kinetics of crystal growth-The case of the 1991-93 Mt. Etna eruption. Contributions to Mineralogy and Petrology, 115, 402-414.

Arzilli, F., Agostini, C., Landi, P., Fortunati, A., Mancini, L., and Carroll, M.R. (2015) Plagioclase nucleation and growth kinetics in a hydrous basaltic melt by decompression experiments. Contributions to Mineralogy and Petrology, 170, 1-16.

Azpiroz, M.D., and Fera´ndez, C. (2003) Characterization of tectono-metamorphic events using crystal size distribution (CSD) diagrams. A case study from the Acebuches metabasites (SW Spain). Journal of Structural Geology, 25, 935-947.

Berger, A., Herwegh, M., Schwarz, J.O., and Putlitz, B. (2011) Quantitative analysis of crystal/grain sizes and their distributions in 2D and 3D. Journal of Structural Geology, 33, 1751-1763.

Boorman, S., Boudreau, A., and Kruger, F.J. (2004) The lower zone-critical zone transition of the bushveld complex: a quantitative textural study. Journal of Petrology, 45, 1209-1235.

Brugger, C.R., and Hammer, J.E. (2010) Crystal size distribution analysis of plagioclase in experimentally decompressed hydrous rhyodacite magma. Earth and Planetary Science Letters, 300, 246-254.

Cabane, H., Laporte, D., and Provost, A. (2005) An experimental study of Ostwald ripening of olivine and plagioclase in silicate melts: implications for the growth and size of crystals in magmas. Contributions to Mineralogy and Petrology, 150, 37-53.

Cashman, K.V. (1993) Relationship between plagioclase crystallization and cooling rate in basaltic melts. Contributions to Mineralogy and Petrology, 113, 126-142.

Cashman, K.V., and Ferry, J.M. (1988) Crystal size distribution (CSD) in rocks and the kinetics and dynamics of crystallization III. Metamorphic crystallization. Contributions to Mineralogy and Petrology, 99, 401-415.

Cashman, K.V., and Marsh, B.D. (1988) Crystal size distribution (CSD) in rocks and the kinetics and dynamics of crystallization II: Makaopuhi lava lake. Contributions to Mineralogy and Petrology, 99, 292-305.

Castro, J.M., Cashman, K.V., and Manga, M. (2003) A technique for measuring 3D crystal size distributions of prismatic microlites in obsidian. American Mineralogist, 88, 1230-1240.

Cheng, L.L., Zeng, L., Ren, Z.Y., Wang, Y., and Luo, Z.H. (2014) Timescale of emplacement of the Panzhihua gabbroic layered intrusion recorded in giant plagioclase at Sichuan Province, SW China. Lithos, 204, 203-219.

DeHoff, R.T. (1991) A geometrically general theory of diffusion controlled coarsening. Acta Metallurgica et Materialia, 39, 2349-2360.

Dunbar, N.W., Jacobs, G.K., and Naney, M.T. (1995) Crystallization processes in an artificial magma: variations in crystal shape, Growth rates and composition with melt cooling history. Contributions to Mineralogy and Petrology, 120, 412-425.

Fornaciai, A., Perinelli, C., Armienti, P., and Favalli, M. (2015) Crystal size distributions of plagioclase in lavas from the July–August 2001 mount etna eruption. Bulletin of Volcanology, 77, 1-15.

Fu, H.F., and Zhu, C.M. (1980) Testing parameters such as temperature, pressure in static super high pressure apparatus. Physic, 9, 193-195 (In Chinese with English abstract).

Gasparik, T. (2003) Phase diagrams for geoscientists: an atlas of the earth's interior. Heidelberg: Springer,

page 463.

Gondé, C., Massare, D., Bureau, H., Martel, C., Pichavant, M., and Clocchiatti, R. (2006) In situ study of magmatic processes: a new experimental approach. High Pressure Research, 26, 243-250.

Hammer, J.E., and Rutherford, M.J. (2002) An experimental study of the kinetics of decompression-induced crystallization in silicic melt. Journal of Geophysical Research: Solid Earth, 107, 1-24.

Hawthorne, F.C., Oberti, R., Martin, R.F., Harlow, G.E., Maresch, W.V., Schumacher, J.C., and Welch, M.D. (2012) Nomenclature of the amphibole supergroup. American Mineralogist, 97, 2031-2048.

Herwegh, M. (2000) A new technique to automatically quantify microstructures of fine grained carbonate mylonites: two step etching combined with SEM imaging and image analysis. Journal of Structural Geology, 22, 391-400.

Higgins, M.D. (1998) Origin of anorthosite by textural coarsening: Quantitative measurements of a natural sequence of textural development. Journal of Petrology, 39, 1307-1323.

Higgins, M.D. (2000) Measurement of crystal size distributions. American Mineralogist, 85, 1105-1116.

Higgins, M.D. (2002a) Closure in crystal size distributions (CSD), verification of CSD calculations, and the significance of CSD fans. American Mineralogist, 87, 171-175.

Higgins, M.D. (2002b) A crystal size-distribution study of the Kiglapait layered mafic intrusion, Labrador, Canada: evidence for textural coarsening. Contributions to Mineralogy and Petrology, 144, 314-330.

Higgins, M.D., and Roberge, J. (2003) Crystal size distribution of plagioclase and amphibole from soufriere hills volcano, montserrat: evidence for dynamic crystallization-textural coarsening cycles. Journal of Petrology, 44, 1401-1411.

Higgins, M.D. (2006a) Quantitative Textural Measurements in Igneous and Metamorphic Petrology. Cambridge University Press, Cambridge, UK, page 41.

Higgins, M.D. (2006b) Verification of ideal semi-logarithmic, lognormal or fractal crystal size distributions from 2D datasets. Journal of Volcanology and Geothermal Research 154, 8-16.

Higgins, M.D., and Chandrasekharam, D. (2007) Nature of sub-volcanic magma chambers, Deccan province, India: evidence from quantitative textural analysis of plagioclase megacrysts in the giant plagioclase

basalts. Journal of Petrology, 48, 885-970.

Higgins, M.D., and Roberge, J. (2007) Three magmatic components in the 1973 eruption of Eldfell volcano, Iceland: evidence from plagioclase crystal size distribution (CSD) and geochemistry. Journal of Volcanology and Geothermal Research, 161, 247-260.

Higgins, M.D. (2011) Textural coarsening in igneous rocks. International Geology Review 53, 354-376.

Jerram, D.A., Mock, A., Davis, G.R., Field, M., and Brown, R.J. (2009) 3D crystal size distributions: a case study on quantifying olivine populations in kimberlites. Lithos, 112, 223-235.

Kirkpatrick, R.J. (1977) Nucleation and growth of plagioclase, Makaopuhi and Alae lava lakes, Kilauea Volcano, Hawaii. Geological Society of America Bulletin, 88, 78-84.

Lentz, R.C.F., and Mcsween, H.Y. (2000) Crystallization of the basaltic shergottites: insights from crystal size distribution (CSD) analysis of pyroxenes. Meteoritics & Planetary Science, 35, 919-927.

Li, D.D., Wang, Y.W., Wang, J.B., Wang, L.J., Long, L., and Liao, Z. (2012) The timing order of mineralization and diagenesis for Xiangshan complex rocks, Xinjiang. Acta Petrologica Sinica, 28, 2103-2112 (In Chinese with English abstract).

Lifshitz, I.M., and Slyozov, V.V. (1961) The kinetics of precipitation from supersaturated solid solutions. Journal of Physics and Chemistry of Solids, 19, 35-50.

Mangan, M.T. (1990) Crystal size distribution systematics and the determination of magma storage times: the 1959 eruption of Kilauea volcano, Hawaii. Journal of Volcanology and Geothermal Research, 44, 295-302.

Marsh, B.D. (1988) Crystal size distribution (CSD) in rocks and the kinetics and dynamics of crystallization I. Theory. Contributions to Mineralogy and Petrology, 99, 277-291.

Marsh, B.D. (1998) On the interpretation of crystal size distributions in magmatic systems. Journal of Petrology, 39, 553-599.

Mills, R.D., and Glazner, A.F. (2013) Experimental study on the effects of temperature cycling on coarsening of plagioclase and olivine in an alkali basalt. Contributions to Mineralogy and Petrology, 166, 97-111.

Mock, A., and Jerram, D.A. (2005) Crystal size distributions (CSD) in three dimensions: insights from the 3D reconstruction of a highly porphyritic rhyolite. Journal of Petrology, 46, 1525-1541.

Morgan, D.J., and Jerram, D.A. (2006) On estimating crystal shape for crystal size distribution analysis. Journal of Volcanology and Geothermal Research, 154, 1-7.

Morgan, G.B., and London, D. (2005) Effect of current density on the electron microprobe analysis of alkali aluminosilicate glasses. American Mineralogist, 90, 1131-1138.

Mujin, M., Nakamura, M., & Miyake, A. (2017) Eruption style and crystal size distributions: crystallization of groundmass nanolites in the 2011 shinmoedake eruption. American Mineralogist, 102, 2367-2380.

Ni, H.W., Keppler, H., Walte, N., Schiavi, F., Chen, Y., Masotta, M., and Li, Z.J. (2014) In situ observation of crystal growth in a basalt melt and the development of crystal size distribution in igneous rocks. Contributions to Mineralogy and Petrology, 167, 1003.

O'Driscoll, B., Stevenson, C.T.E., and Troll, V.R. (2008) Mineral lamination development in layered gabbros of the British palaeogene igneous province: a combined anisotropy of magnetic susceptibility, quantitative textural and mineral chemistry study. Journal of Petrology, 49, 1187-1221.

Orlando, A., D'Orazio, M., Armienti, P., and Borrini, D. (2008) Experimental determination of plagioclase and clinopyroxene crystal growth rates in an anhydrous trachybasalt from Mt Etna (Italy). European Journal of Mineralogy, 20, 653-664.

Piochi, M., Mastrolorenzo, G., and Pappalardo, L. (2005) Magma ascent and eruptive processes from textural and compositional features of Monte Nuovo pyroclastic products, Campi Flegrei, Italy. Bulletin of Volcanology, 67, 663-678.

Pupier, E., Duchene, S., and Toplis, M.J. (2008) Experimental quantification of plagioclase crystal size distribution during cooling of a basaltic liquid. Contributions to Mineralogy and Petrology, 155, 555-570.

Putirka, K. (2016) Amphibole thermometers and barometers for igneous systems and some implications for eruption mechanisms of felsic magmas at arc volcanoes. American Mineralogist, 101, 841–858.

Ridolfi, F., and Renzulli, A. (2011) Calcic amphiboles in calc-alkaline and alkaline magmas:

thermobarometric and chemometric empirical equations valid up to 1,130°C and 2.2 GPa. Contributions to Mineralogy and Petrology, 163, 877-895.

Schiavi, F., Walte, N., and Keppler, H. (2009) First in situ observation of crystallization processes in a basaltic-andesitic melt with the moissanite cell. Geology, 37, 963-966.

Shan, S.M., Wang, R.P., Guo, J., and Li, H.P. (2007) Pressure calibration for the sample cell of YJ-3000t multi anvil press at high temperature and high pressure. Chinese Journal of High Pressure Physics, 21, 367-372 (In Chinese with English abstract).

Silva, M.M.D., Holtz, F., and Namur, O. (2017) Crystallization experiments in rhyolitic systems: the effect of temperature cycling and starting material on crystal size distribution. American Mineralogist, 102, 2284-2294.

Simakin, A.G., and Bindeman, I.N. (2008) Evolution of crystal sizes in the series of dissolution and precipitation events in open magma systems. Journal of Volcanology and Geothermal Research, 177, 997-1010.

Simakin, A.G., Salova, T.P., and Babansky, A.D. (2009) Amphibole crystallization from a water-saturated andesite melt: experimental data at P=2 kbar. Petrology, 17, 591-605.

Smith, P.M., and Asimow, P.D. (2005) Adiabat_1ph: A new public front-end to the MELTS, pMELTS, and pHMELTS models. Geochemistry Geophysics Geosystems, 6, 1-8.

Toramaru, A. (1991) Model of nucleation and growth of crystals in cooling magmas. Contributions to Mineralogy and Petrology, 108, 106-117.

Turner, S., George, R., Jerram, D.A., Carpenter, N., and Hawkesworth, C. (2003) Case studies of plagioclase growth and residence times in island arc lavas from Tonga and the Lesser Antilles, and a model to reconcile discordant age information. Earth and Planetary Science Letters, 214, 279-294.

Vinet, N., and Higgins, M.D. (2011) What can crystal size distributions and olivine compositions tell us about magma solidification processes inside Kilauea Iki lava lake, Hawaii? Journal of Volcanology and Geothermal Research, 208, 136-162.

Vona, A., and Romano, C. (2013) The effects of undercooling and deformation rates on the crystallization

kinetics of Stromboli and Etna basalts. Contributions to Mineralogy and Petrology, 166, 491-509.

Voorhees, P.W. (1992) Ostwald ripening of two-phase mixtures. Annual Review of Materials Science, 22, 197-215.

Xiao, Q.H., Qin, K.Z., Tang, D.M., Su, B.X., Sun, J.Z., Cao, M.J., and Hui, W.D. (2010) Xiangshanxi composite Cu-Ni-Ti-Fe deposit belongs to comagmatic evolution product: Evidences from ore microscopy, zircon U-Pb chronology and petrological geochemistry, Hami, Xinjiang, NW China. Acta Petrologica Sinica , 26, 503-522 (In Chinese with English abstract).

Yang, Z.F. (2012) Combining quantitative textural and geochemical studies to understand the solidification processes of a granite porphyry: shanggusi, east Qinling, China. Journal of Petrology, 53, 1807-1835.

Yang, Z.F., Luo, Z.H., and Lu, X.X. (2010) Quantitative textural analysis of igneous rocks and the kinetics and dynamics of magma solidification processes. Earth Science Frontiers, 17, 246-26 (In Chinese with English abstract).

Zellmer, G.F., Sakamoto, N., Matsuda, N., Iizuka, Y., Moebis, A., and Yurimoto, H. (2016) On progress and rate of the peritectic reaction Fo+SiO_2→En in natural andesitic arc magmas. Geochimica et Cosmochimica Acta, 185, 383-393.

Zhou, W.G., Zhang, B.R., Zhao, Z.D., and Xie, H.S. (1998) Geochemical characteristics and the provenance of cenozoic basic volcanic rocks in western Henan province, China. Journal Mineral Petrology, 18, 51-57 (In Chinese with English abstract).

Zhou, W.G., Hou, W., Zhao, Z.D., Guo, J., Xu, J., and Bai, W.M. (1999) Garnet growth in the early stage of transformation from trachybasalt to eclogite. Acta Mineralogica Sinica, 19, 413-417 (In Chinese with English abstract).

Zieg, M.J., and Marsh, B.D. (2002) Crystal size distributions and scaling laws in the quantification of igneous textures. Journal of Petrology, 43, 85-101.

FIGURE 1. (a-c) BSE images of the "temperature series", multi-anvil runs at uniform pressure 0.6 GPa, crystallization temperatures of 860-970 °C, and run duration 100 hours. (**d-g**) BSE images of the "pressure

series", multi-anvil runs at 0.6-2.6 GPa, uniform crystallization temperature 970 °C, and duration 100 hours. (**h-j**) BSE images of the "time series", multi-anvil runs at uniform crystallization pressure of 0.6 GPa and temperatures of 970 °C and variable run duration 1-60 hours. (**k**) BSE image of piston cylinder at 1.0 GPa, 900 °C, 63 hours. (**l**) The thin photo of the natural diorite. Light gray, *Amp* amphibole; dark, *Gl* glass; white, *Apa* apatite; *Pl* plagioclase. The capital letters *B* and *D* are used to call out backscatter-bright and dark areas of amphibole crystals in image **g**. Note scale bars in each panel; each image was taken at an optimal magnification for the grain sizes typical in that experiment.

FIGURE 2. (**a**) Representative BSE image of an experimental product (RUN#10084-3, 0.6 GPa/1460 °C /970 °C /100 h); (**b**) Threshold binary image with amphibole shown as black and other phases (voids, inclusions, apatite, and glass) as white.

FIGURE 3. (**a**) Representative best-fit shape curves of amphibole crystals in experimental product (10084-3) and diorite (XS-4) (The notation "1.0:1.4:3.4" in the legend gives ratios *S*:*I*:*L* where *S*=Short dimension, *I*=Intermediate dimension, *L*=Long dimension). Other experimental products are similar to 10084-3. (**b**) The mean three-dimensional shape distribution for each experiment and the natural diorite, relative to boundaries established for the habits tabular, equant, prismatic, and bladed. The amphibole is dominantly bladed in most runs. The mean shapeis tabular of amphibole in product of 2.1 GPa and 970 °C and the diorite, and the shape is prismatic in 0.6 GPa and 970 °C. *0.6/860* means 0.6 GPa/970 °C, and *0.6/970/1* means 0.6 GPa/970 °C/1 hour in the legend.

FIGURE 4. CSD plots (logarithmic population density *n* vs. crystal size *L*) of amphibole crystals from experiments (**a, b, c**) and diorite (**d**). Error bars are calculated by CSDCorrections 1.40; when not visible they are smaller than the symbols. Filled symbols are excluded from the regression analysis. The insets in (**a**), (**b**) and (**c**) show the best fitting straight lines along with the open symbols only.

FIGURE 5. Illustration of the influence of textural coarsening on CSD. Textural coarsening following (**a**)**,** the LSW model (Lifshitz and Slyozov 1961) and (**b**), the CN model (Dehoff 1991), this whole figure is cited from Higgins (1998).

FIGURE 6. Relations between temperature, pressure and the growth rate of amphibole from hydrous basaltic melt. The plane represents the result of linear regression, equation (5). When not visible, the error bars (1σ) are smaller than the symbols.

This is a preprint, the final version is subject to change, of the American Mineralogist (MSA)
Cite as Authors (Year) Title. American Mineralogist, in press.
DOI: https://doi.org/10.2138/am-2019-6759

TABLE 1. Chemical composition of the starting material (10084, weight percent) [a]

SiO_2	Al_2O_3	TiO_2	MgO	Fe_2O_3	FeO	MnO	CaO	Na_2O	K_2O	P_2O_5	CO_2	H_2O^+	Total	δ [b]
47.8	14.13	2.48	6.44	7.57	3.53	0.16	8.40	3.90	1.26	0.90	0.02	3.33	99.92	5.55

Notes: [a] Sample number 10084 from Zhou et al. 1998.

[b] Rittman index, $\delta = (Na_2O+K_2O)^2/(SiO_2-43)$.

This is a preprint, the final version is subject to change, of the American Mineralogist (MSA)
Cite as Authors (Year) Title. American Mineralogist, in press.
DOI: https://doi.org/10.2138/am-2019-6759

TABLE 2. Run conditions and phase compositions of experimental glass and amphibole in experimental products and natural diorite

Run# [a]	10084-1		10084-2		10084-3		10084-4		10084-5		10084-6		10084-7	
T(°C) [c]	1460/860		1460/915		1460/970		1490/970		1515/970		1540/970		1570/970	
P(GPa)	0.6		0.6		0.6		1.1		1.6		2.1		2.6	
T(h)	100		100		100		100		100		100		100	
Phase [d]	Amp+Ab+Apa+Gl		Amp+Apa+Gl		Amp+Apa+Gl		Amp+Apa+Gl		Amp+Apa+Gl		Amp+Apa+Sp+Gl		Amp+Apa+Sp+Gl	
n [e]	Amp(4)	Gl(4)	Amp(4)	Gl(4)	Amp(5)	Gl(7)	Amp(5)	Gl(4)	Amp(4)	Gl(4)	Amp(11)	Gl(6)	Amp(6)	Gl(4)
SiO_2 [f]	43(3)	60(3)	41(2)	62.0(8)	40.9(7)	58.4(6)	40.5(9)	58.4(3)	39.2(5)	61.9(6)	40(1)	60.6(8)	39.7(3)	60.7(9)
Al_2O_3	12(3)	22(2)	14.3(8)	19.5(4)	13.5(4)	18.3(2)	14.6(5)	19.1(3)	15.7(7)	18.05(9)	16.1(8)	18.2(1)	16(1)	19.1(4)
TiO_2	3.1(8)	0.11(6)	3.4(3)	0.48(4)	3.5(4)	0.82(6)	3.7(4)	0.76(8)	3.9(1)	0.73(3)	3.1(5)	0.72(5)	3.2(4)	0.81(8)
Cr_2O_3	0.14(9)	0.08(7)	0.05(3)	0.04(3)	0.2(1)	0.08(8)	0.04(3)	0.02(1)	0.04(4)	0.02(1)	0.08(4)	0.1(1)	0.06(2)	0.03(1)
MgO	11.4(4)	0.04(3)	10.3(8)	0.4(1)	10.9(5)	1.20(8)	11(1)	0.7(2)	8.6(6)	0.53(3)	10.2(5)	0.67(5)	9.5(2)	0.42(3)
NiO	0.02(1)	0.02(0)	0.03(0)	0.01(1)	0.02(2)	0.02(1)	0.01(1)	0.01(0)	0.02(2)	0.03(0)	0.04(2)	0.01(1)	0.02(1)	0.03(1)
FeO [g]	13(1)	0.6(2)	13.0(8)	2.9(3)	14.0(7)	6.9(2)	13.2(8)	4.4(9)	14.9(4)	3.4(1)	12(1)	3.2(1)	13(2)	2.8(2)
MnO	0.23(8)	0.04(3)	0.19(2)	0.07(2)	0.18(5)	0.13(4)	0.18(1)	0.11(3)	0.17(2)	0.06(2)	0.16(6)	0.08(1)	0.17(3)	0.06(2)
CaO	12(3)	6(2)	10.6(9)	2.5(2)	10.3(2)	4.1(2)	10.7(3)	3.1(1)	9.9(2)	2.03(2)	10(1)	2.4(2)	10.7(3)	2.0(2)
Na_2O	2.4(7)	7 (2)	2.8(1)	6.58(3)	2.82(7)	5. 1(2)	2.59(8)	5.8(2)	3.02(4)	5.10(5)	3.1(1)	5.7(2)	2.9(2)	4.6(1)
K_2O	1.1(3)	1.3(7)	1.4(2)	1.4(2)	1.0(2)	1.21(4)	1.7(6)	2.8(3)	1.9(2)	1.80(9)	1.9(6)	2.0(1)	1.7(5)	2.2(3)
Total	97.89	97.75	97.44	96.01	97.24	96.20	97.76	95.29	97.23	93.59	96.39	93.71	96.84	92.74

This is a preprint, the final version is subject to change, of the American Mineralogist (MSA)
Cite as Authors (Year) Title. American Mineralogist, in press.
DOI: https://doi.org/10.2138/am-2019-6759

TABLE 2. continued

Run# [a]	10084-8		10084-9		10084-10		R461		XS-4 [b]
T(°C) [c]	1460/970		1460/970		1460/970		1370/900		
P(GPa)	0.6		0.6		0.6		1.0		Diorite
T(h)	1		10		60		63		
Phase [d]	Amp+Ab+Apa+Gl		Amp+Apa+Gl		Amp+Apa+Gl		Amp+Ab+Apa+Gl		Amp+Pl
n [e]	Amp(5)	Gl(16)	Amp(12)	Gl(15)	Amp(9)	Gl(11)	Amp(10)	Gl(7)	Amp(3)
SiO_2 [f]	41(1)	55.5(9)	40(1)	58.5(7)	41(1)	56.1(8)	41.4(8)	67.3(3)	45.6(9)
Al_2O_3	13.2(3)	16.3(5)	13.4(6)	18.3(2)	12.3(2)	17.1(1)	12.7(2)	15.5(4)	9.0(4)
TiO_2	3.6(5)	1.1(1)	4.0(5)	0.50(4)	4.0(5)	1.2(1)	3.6(3)	0.35(2)	2.4(1)
Cr_2O_3	0.02(1)	0.01(0)	0.04(2)	0	0.06(2)	0.01(0)	0.02(1)	0	0.06(4)
MgO	10.4(6)	1.7(1)	11(1)	1.3(1)	13.2(7)	1.7(1)	9.4(7)	0.31(1)	13.7(2)
NiO	0.02(1)	0.01(0)	0.02(1)	0	0.05(2)	0	0.02(2)	0	0.02(1)
FeO [g]	14.1(4)	9.0(5)	13.3(8)	6.5(2)	11.1(8)	7.7(2)	15.7(8)	2.42(9)	11.6(6)
MnO	0.18(3)	0.16(3)	0.17(3)	0.13(2)	0.14(2)	0.16(1)	0.21(3)	0.03(2)	0.22(3)
CaO	10.9(5)	4.2(3)	11.6(5)	5.3(3)	11.8(4)	6.5(3)	10.8(4)	1.41(7)	10.7(1)
Na_2O	2.9(2)	4.3(5)	2.9(1)	4.9(1)	2.8(1)	4.3(1)	2.63(7)	6.0(3)	3.1(9)
K_2O	1.0(2)	4.1(3)	0.7(1)	2.3(1)	0.7(1)	2.0(1)	0.62(5)	2.5(1)	0.4(1)
Total	97.24	96.33	97.68	97.68	97.29	96.73	97.14	95.78	96.83

TABLE 2. continued

10084-7 [h]	Amp bright	Amp dark	Amp bright	Amp dark
SiO_2	39.36	39.73	39.62	40.05
Al_2O_3	16.67	14.81	16.98	15.10
TiO_2	3.83	3.43	3.23	3.00
Cr_2O_3	0.04	0.08	0.05	0.09
MgO	9.32	9.65	9.33	9.71
NiO	0.02	0.01	0.04	0.01
FeO	13.96	11.89	13.99	11.28
MnO	0.20	0.13	0.18	0.18
CaO	10.60	11.26	10.56	10.43
Na_2O	3.12	2.66	3.19	2.90
K_2O	1.20	2.34	1.29	1.89
Total	98.31	95.97	98.45	94.63

Notes: [a] Experimental run and sample number.

[b] The natural diorite.

[c] Melting temperature and crystallization temperature.

[d] Abbreviations of phases: *Amp* amphibole, *Apa* apatite, *Sp* spinel, *Ab* albite, *Gl* glass, *Pl* plagioclase.

[e] Number of analyses.

[f] Wt.% oxides, values in parentheses are standard deviations, thus, *43(3)*, *3.1(8)*, *0.14(9)* should be read as 43±3, 3.1±0.8, 0.14±0.09, respectively.

[g] Total iron as FeO.

[h] see Fig. 1g.

This is a preprint, the final version is subject to change, of the American Mineralogist (MSA)
Cite as Authors (Year) Title. American Mineralogist, in press.
DOI: https://doi.org/10.2138/am-2019-6759

TABLE 3. Crystal chemical formulae of amphibole analyses

Run# [a]	10084-1	10084-2	10084-3	10084-4	10084-5	10084-6	10084-7	10084-8	10084-9	10084-10	R461	XS-4
Si	6.39	6.16	6.11	6.03	5.93	6.03	5.96	6.22	6.04	6.16	6.23	6.72
Al	1.61	1.84	1.89	1.97	2.07	1.97	2.04	1.78	1.96	1.85	1.77	1.28
∑T [b]	8	8	8	8	8	8	8	8	8	8	8	8
Ti	0.35	0.38	0.39	0.42	0.44	0.35	0.38	0.42	0.46	0.45	0.41	0.27
Al	0.37	0.66	0.48	0.59	0.73	0.87	0.78	0.46	0.43	0.32	0.49	0.28
Cr	0.02	0.01	0.02	0	0.01	0.01	0.01	0.00	0.01	0.01	0	0.06
Fe^{3+}	0	0	0.15	0.03	0.01	0	0	0	0	0	0.04	0
Mn^{2+}	0.03	0.02	0	0.01	0.02	0.02	0.02	0.02	0.02	0.02	0.01	0.01
Fe^{2+}	1.63	1.61	1.55	1.62	1.88	1.45	1.61	1.83	1.43	1.64	1.94	1.37
Mg	2.55	2.28	2.42	2.33	1.93	2.27	2.13	2.17	2.58	2.49	2.12	3.00
∑C	4.95	4.97	5	5	5	4.98	4.93	4.91	4.93	4.93	5	4.99
Mn^{2+}	0	0	0.02	0.02	0.01	0	0	0	0	0	0.02	0.01
Fe^{2+}	0	0	0.06	0	0	0	0	0	0	0	0	0
Ca	1.86	1.70	1.65	1.71	1.60	1.59	1.72	1.81	1.88	1.90	1.74	1.70
Na	0.14	0.30	0.27	0.28	0.40	0.41	0.28	0.19	0.12	0.10	0.23	0.28
∑B	2	2	2	2	2	2	2	2	2	2	2	2
Na	0.55	0.50	0.55	0.47	0.49	0.48	0.59	0.67	0.73	0.72	0.54	0.61
K	0.21	0.26	0.19	0.32	0.36	0.37	0.32	0.19	0.13	0.13	0.12	0.08
∑A	0.75	0.76	0.73	0.79	0.85	0.84	0.91	0.86	0.86	0.85	0.65	0.69
O (non-W) [c]	22	22	22	22	22	22	22	22	22	22	22	22
OH	2	2	2	2	2	2	2	2	2	2	2	2
∑W	2	2	2	2	2	2	2	2	2	2	2	2
Sum T,C,B,A	15.70	15.74	15.74	15.79	15.85	15.82	15.84	15.77	15.79	15.79	15.65	15.69
Mg# [d]	61	59	58	56	50	58	57	57	59	60	52	69
Calcic Amphibole [e]	Ti-rich Pargasite	Ti-rich Pargasite	Ti-rich Pargasite	Ti-rich Pargasite	Ti-rich Sadanagaite	Ti-rich Sadanagaite	Sadanagaite	Ti-rich Pargasite	Ti-rich Pargasite	Ti-rich Pargasite	Ti-rich Pargasite	Pargasite

Calculation according to recommendations of IMA-CNMNC (Hawthorne et al. 2012). The general formula of amphibole is $AB_2C_5T_8O_{22}W_2$.

Notes: [a] Experimental run and sample number.

[b] $\sum$T expresses the total number of cations in T site of Amphibole formula; $\sum$A, $\sum$B, $\sum$C, $\sum$W are defined likewise for the other sites.

[c] Oxygen in the formula but not in W site.

[d] $Mg^{\#}$ is the molar ratio of Mg/(Mg+Fe)*100, all Fe assumed to be Fe^{2+}.

[e] All amphiboles are classified as calcic amphibole [$^{B}(Ca+\sum M^{2+}) / \sum B \geq 0.75$, $^{B}Ca / \sum B \geq {}^{B}\sum M^{2+} / \sum B$]. Species assignments are given for each experimental product and the natural diorite.

TABLE 4. Textural parameters of amphibole in experiments and diorite

Run[#]	Best 3D shape [a]	Round-ness [b]	Area (mm^2)[c]	Area (mm^2)[d]	Number [e]	Range (mm) [f]	L_{max} (mm)	L'_{max} (mm)	$L_{av.}$ (mm) [g]	Intercept	Slope [h]	R^2 [i]
10084-1	1:2:5	0.6	0.40	0.15	3508	0.001-0.09	0.09	0.02	0.01	20.3±0.2	-151±13	0.97
10084-2	1:1.6:5	0.6	0.95	0.39	1598	0.001-0.16	0.13	0.04	0.02	16.0±0.2	-48.9±3.6	0.98
10084-3	1:1.4:3.4	0.5	6.46	2.28	766	0.005-0.42	0.39	0.14	0.08	11.9±0.3	-21.0±1.8	0.98
10084-4	1:1.9:3.2	0.5	6.85	3.31	653	0.02-0.51	0.44	0.12	0.12	11.7±0.5	-20.8±3.3	0.93
10084-5	1:2.9:6	0.5	4.70	2.55	222	0.02-0.73	0.63	0.15	0.20	10.2±0.6	-11.2±1.9	0.92
10084-6	1:2.5:3.4	0.5	6.46	3.74	197	0.02-0.95	0.85	0.22	0.21	8.8±0.2	-10.0±0.8	0.97
10084-7	1:1.6:5	0.6	6.97	3.77	265	0.01-1.04	0.94	0.23	0.23	8.3±0.2	-6.7±0.4	0.99
10084-8	1:1.7:4.5	0.5	0.06	0.03	6055	0.0001-0.04	0.03	0.005	0.003	24.2±0.1	-363±13	0.99
10084-9	1:1.5:2.8	0.6	1.36	0.59	2190	0.0005-0.3	0.19	0.04	0.02	16.3±0.1	-64±2	0.99
10084-10	1:1.4:4.3	0.5	1.85	0.72	2860	0.0005-0.4	0.32	0.05	0.02	13.6±0.5	-30.3±2.9	0.96
R461	1:2:3.4	0.6	0.20	0.09	3397	0.001-0.04	0.04	0.009	0.01	20.2±0.2	-180±11	0.98
XS-4	1:1.7:2.2	0.4	620	160	192	0.01-3.40	3.27	2.16	1.17	0.3±0.1	-1.7±0.1	0.99

Notes: [a] Best 3D crystal habit of amphibole from CSDslice (Morgan and Jerram 2006).

[b] Average roundness of analyzed grains.

[c] Area of thin section analyzed.

[d] Area of amphibole within analyzed area.

[e] Number of grains analyzed.

[f] Size range of amphibole crystal long axes.

[g] L_{max} is the average of the four largest intersection lengths of amphiboles in each product; L'_{max} is the corresponding average of four largest widths; $L_{av.}$ is the average length of all amphibole crystal long axes.

[h] *Intercept* and *slope* are calculated using CSDCorrections 1.40 (see text).

[i] Correlation coefficient of the regression line in CSD plots.

This is a preprint, the final version is subject to change, of the American Mineralogist (MSA)
Cite as Authors (Year) Title. American Mineralogist, in press.
DOI: https://doi.org/10.2138/am-2019-6759

TABLE 5. Amphibole growth rates

Run#	Growth rate (mm/s)		
	G_{CSD}	G_{max}	$G_{av.}$
10084-1	1.8(2) E−8	2.50(8) E−7	3(2) E−8
10084-2	5.7(4) E−8	3.6(6) E−7	7(5) E−8
10084-3	1.3(1) E−7	1.08(8) E−6	2.3(1) E−7
10084-4	1.4(2) E−7	1.2(2) E−6	3.2(1) E−7
10084-5	2.5(5) E−7	1.8(2) E−6	5.5(3) E−7
10084-6	2.8(3) E−7	2.4(2) E−6	6.1(4) E−7
10084-7	4.2(3) E−7	2.6(2) E−6	6.4(4) E−7
10084-8	7.6(3) E−7	10(2) E−6	8(4) E−7
10084-9	4.3(1) E−7	6(1) E−6	6(3) E−7
10084-10	1.5(2) E−7	1.5(2) E−6	10(2) E−8
R461	2.4(1) E−8	1.8(2) E−7	4(2) E−8
XS-4	1.6 E−9 -5.7 E−8	8.9 E−8 -5.6 E−7	3.1 E−8 -1.7 E−7

The growth rate (G_{CSD}) was calculated from *Eq. (4)*. The G_{max} and $G_{av.}$ are growth rates based on largest and average crystal sizes. The values in parentheses are one standard deviation. The crystallization parameters of amphibole for sample XS-4 have a range because the growth rate is calculated by *Eq. (5)*, *(6)*, and *(7)*. *7(2) E+8*, *1.2(3) E+1*, *2.50(8) E−7* should be read as 7(±2) E+8, 1.2(±0.3) E+1, 2.50(±0.08) E−7, respectively.

This is a preprint, the final version is subject to change, of the American Mineralogist (MSA)
Cite as Authors (Year) Title. American Mineralogist, in press.
DOI: https://doi.org/10.2138/am-2019-6759

FIGURE 1

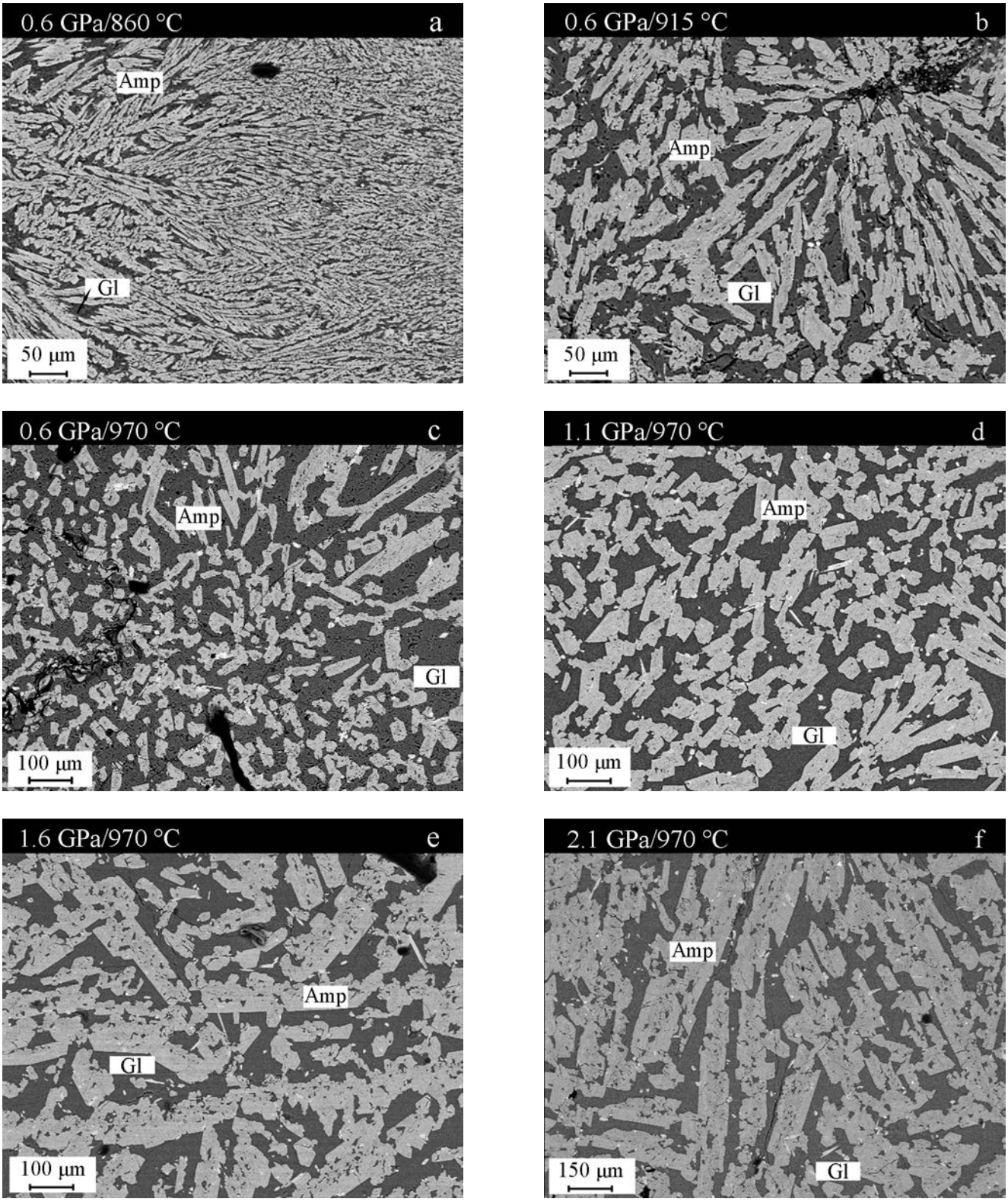

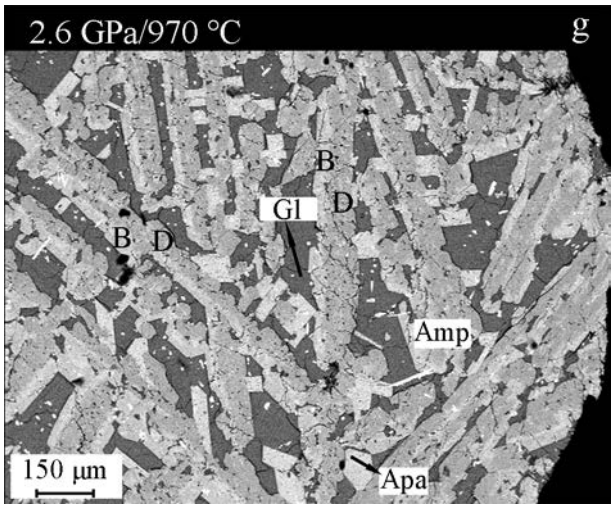

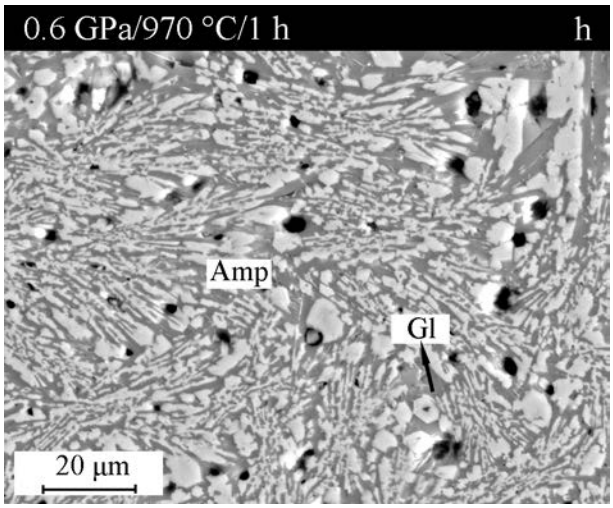

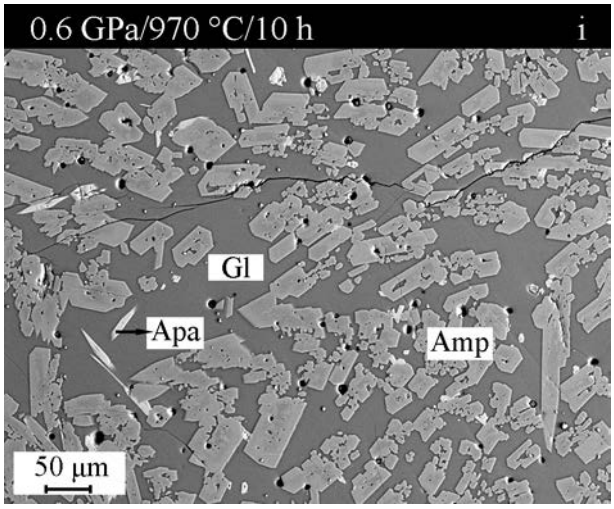

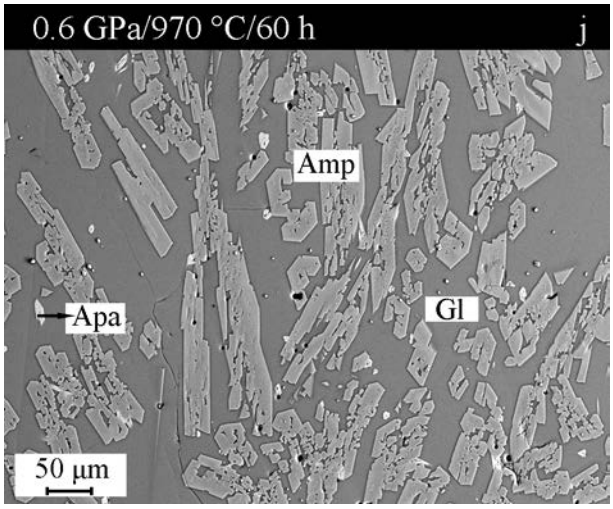

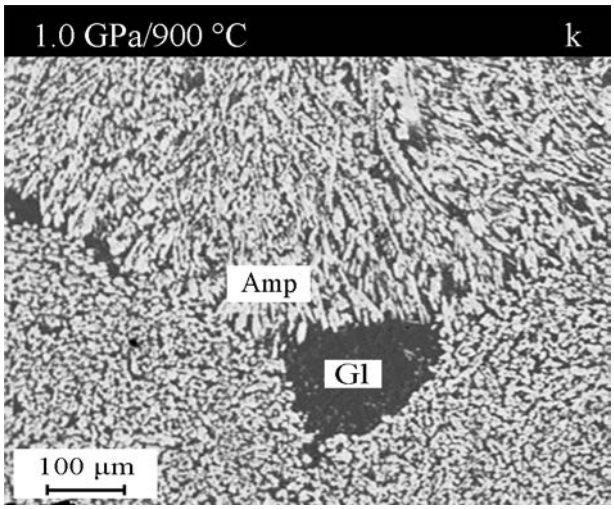

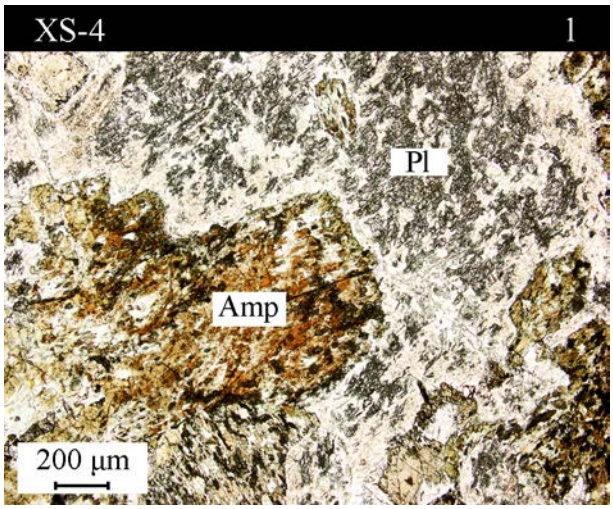

This is a preprint, the final version is subject to change, of the American Mineralogist (MSA)
Cite as Authors (Year) Title. American Mineralogist, in press.
DOI: https://doi.org/10.2138/am-2019-6759

FIGURE 2

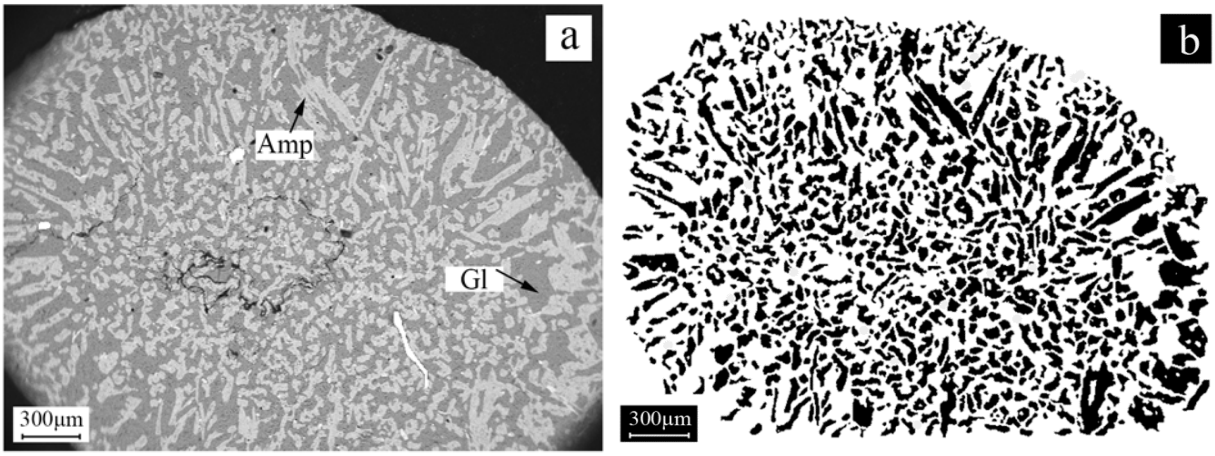

FIGURE 3

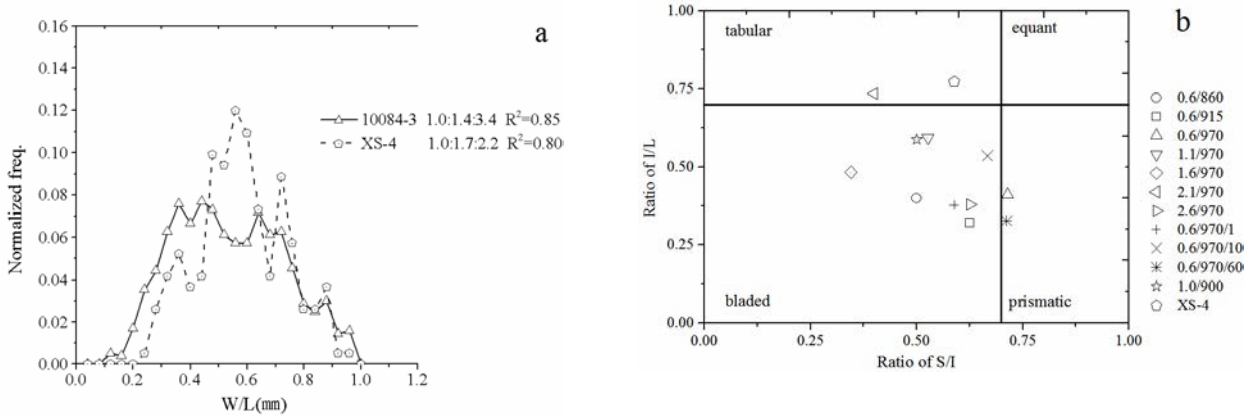

FIGURE 4

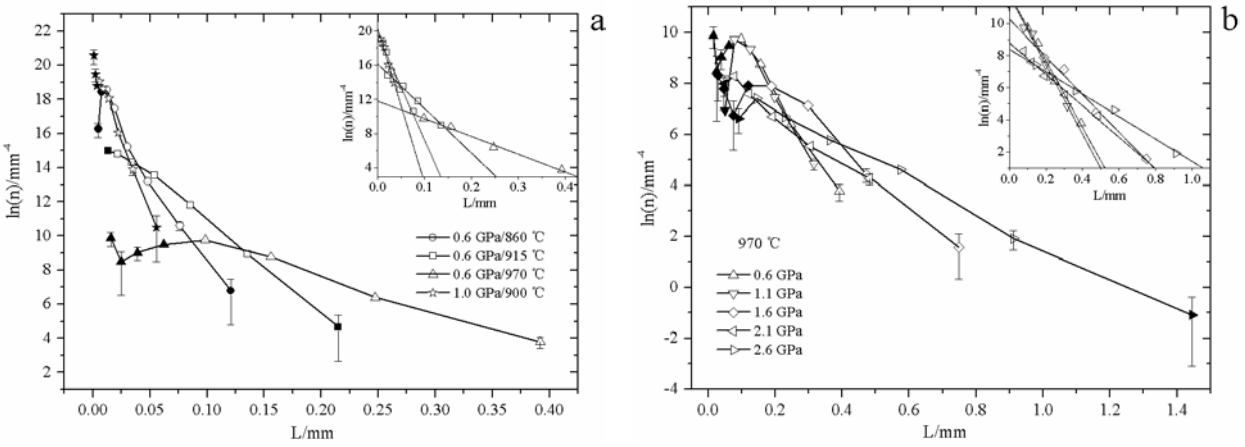

This is a preprint, the final version is subject to change, of the American Mineralogist (MSA)
Cite as Authors (Year) Title. American Mineralogist, in press.
DOI: https://doi.org/10.2138/am-2019-6759

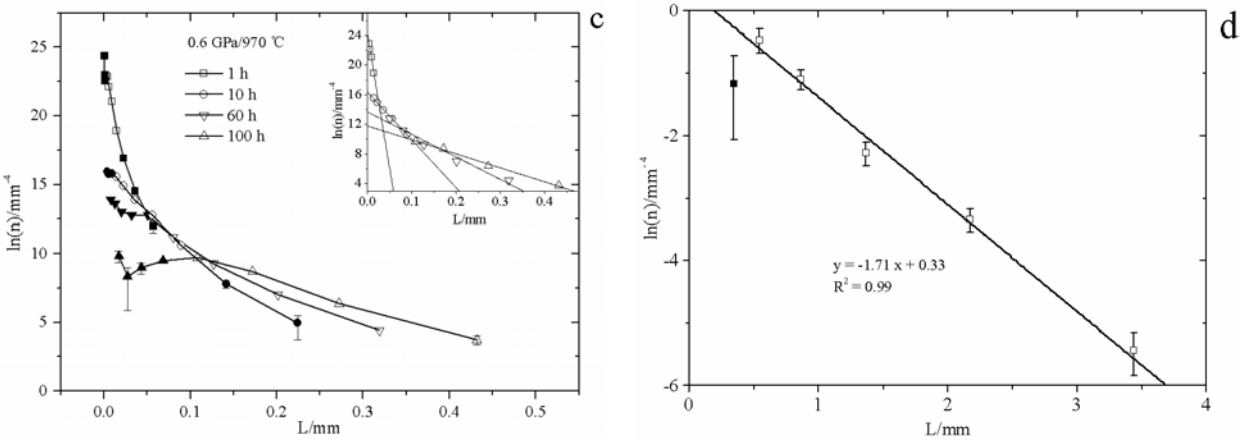

FIGURE 5

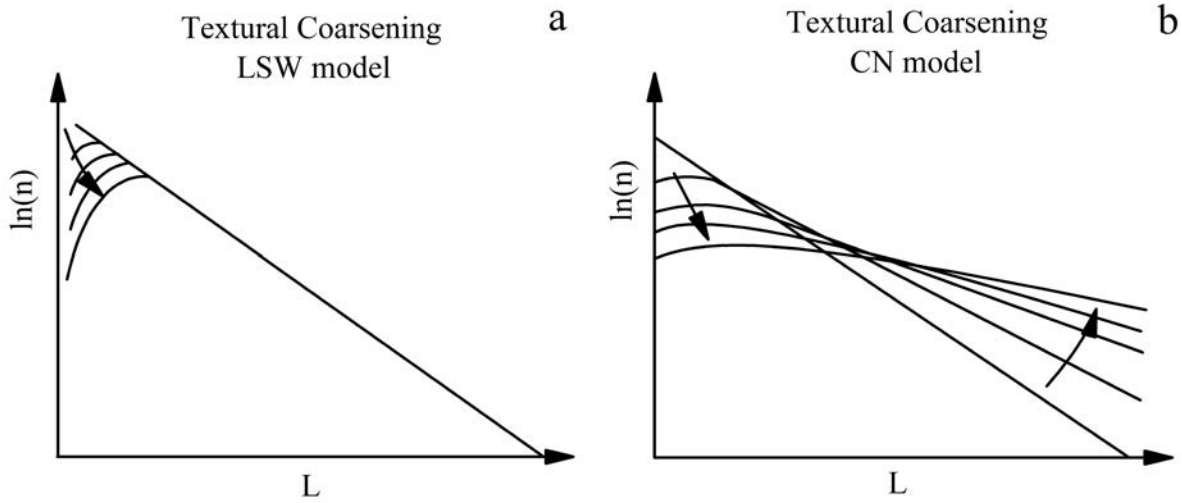

This is a preprint, the final version is subject to change, of the American Mineralogist (MSA)
Cite as Authors (Year) Title. American Mineralogist, in press.
DOI: https://doi.org/10.2138/am-2019-6759

FIGURE 6